# TREM2-dependent lipid droplet biogenesis in phagocytes is required for remyelination

Garyfallia Gouna[1,2] ![ORCID], Christian Klose[3] ![ORCID], Mar Bosch-Queralt[1,2] ![ORCID], Lu Liu[4] ![ORCID], Ozgun Gokce[4,5] ![ORCID], Martina Schifferer[2,5] ![ORCID], Ludovico Cantuti-Castelvetri[1,2]* ![ORCID], and Mikael Simons[1,2,5]* ![ORCID]

**Upon demyelinating injury, microglia orchestrate a regenerative response that promotes myelin repair, thereby restoring rapid signal propagation and protecting axons from further damage. Whereas the essential phagocytic function of microglia for remyelination is well known, the underlying metabolic pathways required for myelin debris clearance are poorly understood. Here, we show that cholesterol esterification in male mouse microglia/macrophages is a necessary adaptive response to myelin debris uptake and required for the generation of lipid droplets upon demyelinating injury. When lipid droplet biogenesis is defective, innate immune cells do not resolve, and the regenerative response fails. We found that triggering receptor expressed on myeloid cells 2 (TREM2)–deficient mice are unable to adapt to excess cholesterol exposure, form fewer lipid droplets, and build up endoplasmic reticulum (ER) stress. Alleviating ER stress in TREM2-deficient mice restores lipid droplet biogenesis and resolves the innate immune response. Thus, we conclude that TREM2-dependent formation of lipid droplets constitute a protective response required for remyelination to occur.**

## Introduction

Tissue injury is followed by a repair process, which attempts to reestablish tissue structure and function, but within the central nervous system (CNS), persistent and sometimes even progressive neurological deficits remain (Franklin and Ffrench-Constant, 2017). Remyelination is an example of a regenerative process that can occur in diseases such as multiple sclerosis but often fails during the progressive phase of the disease (Dendrou et al., 2015; Reich et al., 2018). Identifying the mechanisms that determine the outcome of lesions is therefore an important goal for the design of regenerative medicines (Plemel et al., 2017). Microglia are a prime therapeutic target because they represent a key cellular component of the regenerative response, which occurs in distinct phases, starting with microglia activation, followed by phenotype adaptation, and ending with the resolution of the response (Cunha et al., 2020; Miron et al., 2013). We know very little about the underlying checkpoints that drive the sequence of these regenerative responses. A key function of microglia is to clear cellular debris, a process that is necessary to pave the way for the regenerative response and for inflammation resolution (Kotter et al., 2006; Lampron et al., 2015; Lloyd and Miron, 2019). In demyelinating lesions, myelin debris

clearance poses a challenge to microglia, as myelin is lipid-rich and consists of large amounts of cholesterol, which cannot be degraded and therefore requires mechanisms for storage and efflux (Cantuti-Castelvetri et al., 2018; Bogie et al., 2020; Berghoff et al., 2021; Bosch-Queralt et al., 2021). We have previously shown that the cholesterol efflux pathway is insufficiently activated in phagocytes within demyelinating lesions of aged mice (Cantuti-Castelvetri et al., 2018). We found that cholesterol-rich myelin debris can overwhelm the efflux capacity of phagocytes, resulting in the accumulation of foamy microglia with large amounts of lipid droplets and cholesterol crystals in lesions. Here, we aim to identify the molecules that control lipid metabolism in microglia in demyelinating lesions. Triggering receptor expressed on myeloid cells 2 (TREM2), an immunoglobulin superfamily cell surface receptor that is specifically expressed in microglia in the CNS, is one key signaling pathway for microglia activation (Deczkowska et al., 2018; Lewcock et al., 2020). Upon activation by lipid ligands, TREM2 signals through its associated immunoreceptor tyrosine-based activation motif (ITAM)–containing adapter protein TYRO protein tyrosine kinase–binding protein (DAP12) to modulate

proliferation, immune responses, phagocytic capacity, and lipid metabolism. Previous work has shown that TREM2-null microglia fail to acquire an activated transcriptional signature upon various neuropathological insults in mice, resulting in defects in debris clearance (Cantoni et al., 2015; Poliani et al., 2015). However, there remains an incomplete understanding of TREM2-dependent lipid processing after tissue injury. To address this question, we use a toxin-based model in which we locally inject the toxin into the CNS of mice to induce injury to myelin. As expected, lesion recovery was impaired, but surprisingly, TREM2-deficient mice failed to develop foamy microglia with lipid droplets in lesions. Lipid droplets arise at the ER through localized lipogenesis (Walther et al., 2017), but TREM2-deficient microglia developed ER stress, and alleviating this response restored lipid droplet formation. One of the characteristics of lipid droplets is their capacity to buffer excess lipids, but they have also been associated with cellular damage pathways. To determine the role of lipid droplet formation in remyelination, we used mice deficient in acyl-CoA:cholesterol acyltransferase (ACAT; soat1/Acat), which is required for the esterification of cellular cholesterol with fatty acids. Upon demyelinating injury, ACAT-deficient mice failed to develop lipid droplet–loaded foamy microglia and showed a marked impairment of lesion recovery. Thus, our data provide evidence that TREM2-dependent formation of lipid droplets represents a protective response required for remyelination to occur.

## Results and discussion
### TREM2 is required for lipid droplet biogenesis and remyelination
To elucidate the role of TREM2 in myelin clearance, we employed a toxin-based model of demyelination in which lysolecithin (LLC) creates a demyelinated lesion within 4 d postinjection (dpi), followed by lesion repair. Using transmission electron microscopy (TEM), we first quantified remyelination in WT and TREM2-deficient mice (TREM2 KO) in 21-dpi lesions and observed fewer myelinated axons and higher g-ratios (the ratio of the inner axonal diameter to the total outer diameter) in TREM2 KO lesions (Fig. 1, A–C). Furthermore, using antibodies against adenomatous polyposis coli (APC; clone CC1), fewer oligodendrocytes were detected in 21-dpi lesions of TREM2 KO mice compared with control, indicating defective lesion repair in TREM2 KO animals (Fig. S1, A and B) as previously described (Cantoni et al., 2015; Poliani et al., 2015). TEM analyses revealed a marked accumulation of myelin debris with honeycomb-like appearance in 21-dpi TREM2 KO lesions (Fig. S1, C and D). Further characterization of the lesions showed that TREM2 KO and WT 4-dpi lesions were of similar size but with a lower number of allograft inflammatory factor 1 (IBA1+) cells in TREM2 KO (Fig. S1, E and F; and Fig. 2, A and B). Microglia/macrophages assessed at additional time points revealed that IBA1+ cell density decreased in WT lesions with time but not in TREM2 KO lesions, pointing to impaired innate immune cell resolution in TREM2 KO mice (Fig. 2, A and B). We found no significant differences in the percentage of galectin-3 (Lgals3 or MAC2) MAC2+/IBA1+ cells, in the number of CD11b+CD45hi cells and in the density of glial fibrillary acidic protein (GFAP+) astrocytes in lesions (Fig. S1, G–J).

To determine the underlying mechanism of defective innate immune cell resolution, we focused on the formation of foamy microglia, which form between 14 and 21 dpi in parallel with the regenerative response. Surprisingly, significantly fewer foamy microglia, characterized by numerous lipid droplets, were observed within TREM2 KO lesions (Fig. 1, A and D). As cholesterol-rich myelin fragments are degraded in the lysosomal system, free cholesterol is released and esterified for storage in lipid droplets. The lack of lipid droplets could be explained by a delay in lipid droplet formation. However, our TEM analysis showed that foamy phagocytes were absent in TREM2 KO, even in lesions at 62 dpi (Fig. 1, A and D). The lack of foamy microglia in TREM2 KO was confirmed by immunohistochemistry (IHC) using antibodies against perilipin 2 (PLIN2), a structural component of lipid droplets, and IBA1. In line with our ultrastructural analysis, the number of IBA1+PLIN2+ cells increased in WT lesions at 21 and 62 dpi but not in TREM2 KO lesions (Fig. 2, A and C). In addition, IHC analysis for TREM2 revealed that 70% of PLIN2+IBA1+ cells also colabeled for TREM2 (Fig. 2 D).

We have previously shown that myelin debris overloading of microglia can result in the transition of cholesterol into its crystalline form, which triggers lysosomal rupture and inflammasome stimulation (Cantuti-Castelvetri et al., 2018). However, by combining laser reflection and fluorescence confocal microscopy (reflection microscopy), we found that IBA1+ cells contained fewer cholesterol crystals in lesions of TREM2 KO compared with WT mice, indicating that cholesterol crystals cannot account for the poor lesion regeneration of TREM2 KO mice (Fig. 2 E).

To determine whether the deficiency of TREM2 leads to defective lipid droplet formation, postnatal and adult microglia were isolated and cultured with myelin debris for 8 or 24 h. Immunofluorescence analyses using antibodies against PLIN2 showed that lipid droplets accumulated in myelin-treated WT microglia at 8 h and to an even a greater extent at 24 h. In contrast, the number of lipid droplets formed by TREM2 KO cells was significantly lower and never reached the levels of WT microglia (Fig. 3, A–C). To provide further evidence for defective lipid droplet biogenesis in TREM2 KO microglia, we performed Western blot experiments and found that myelin debris treatment triggered the expression of PLIN2 in WT but not TREM2 KO microglia (Fig. 3, D and E). Furthermore, RT-PCR for soat1/Acat, the enzyme responsible for cholesterol esterification, mice showed a twofold increase in WT but not TREM2 KO microglia (Fig. 3 F). To explore further the impaired biogenesis of lipid droplets in TREM2 KO microglia, we performed an untargeted lipidomic analysis on myelin debris–treated microglia (Fig. 3 G). As expected, myelin debris treatment induced cholesterol accumulation in both WT and TREM2 KO microglia. However, cholesterol was mostly esterified in WT microglia, while a larger fraction remained as free cholesterol in TREM2 KO cells. Interestingly, myelin treatment induced a distinct lipid profile in TREM2 KO cells characterized by the deficiency of lysophosphatidylcholine (LPC), lysophosphatidylserine (LPS), and lysophosphatidylethanolamine (LPE). Furthermore, triglycerides, another major component of lipid droplets, were generated to a lesser extent in TREM2 KO compared with WT microglia. TREM2 KO microglia accumulated a larger amount
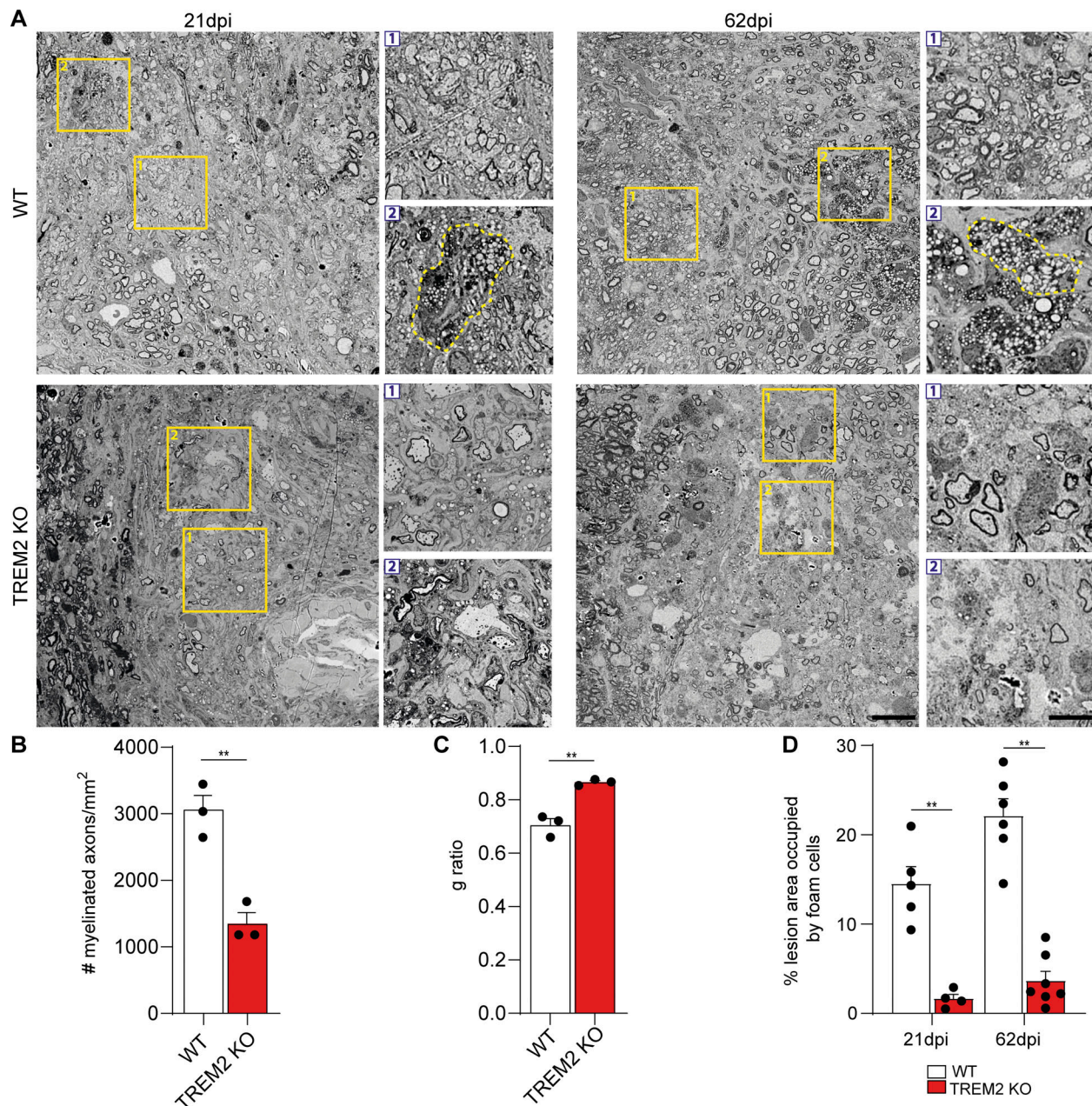
Gouna et al.
Lipid droplet biogenesis required for remyelination

Journal of Experimental Medicine
https://doi.org/10.1084/jem.20210227

2 of 12

Figure 1. **TREM2 is required for lipid droplet biogenesis and remyelination. (A)** Scanning electron microscopic images of 21- and 62-dpi lesions from WT and TREM2 KO mice. Zoomed-in images are provided by areas marked by yellow boxes. Box 1 highlights remyelination and box 2 highlights foam cells (yellow dashed lines) in WT lesions. Poor remyelination and absence of foam cells are shown by boxes 1 and 2 in TREM2 KO lesions. **(B and C)** Quantification of the density of myelinated axons and g-ratio of 21-dpi lesions of WT and TREM2 KO mice. **(D)** Quantification of the percent area of the lesion occupied by foam cells in 21-dpi lesions of WT and TREM2 KO mice. Scale bars, 10 µm for the large image and 2 µm for the zoomed-in image. $n$ = 3–4 animals per condition for A–C; $n$ = 4–7 lesions per condition for D. For the g-ratio analysis, a minimum of 250 axons per condition were analyzed. *, $P < 0.05$; **, $P < 0.01$.

of phosphatidic acid, a precursor in the formation of tri-acylglycerols (TAGs) and phospholipids. Together, our results show that TREM2 is required for the synthesis of cholesterol esters and TAGs for lipid droplet biogenesis after myelin debris uptake.

## Cholesterol esterification is necessary for remyelination

To determine whether the impaired cholesterol esterification could represent one reason for poor remyelination, we induced LLC lesions in ACAT KO mice. Electron microscopic analysis of 21-dpi lesions confirmed that no lipid droplets were formed in ACAT KO animals, proving that esterification of cellular cholesterol with fatty acids is required for lipid droplet formation in phagocytes after demyelinating injury (Fig. 4, A and B; and Fig. S2 A). Analysis of semithin sections and TEM images showed that remyelination was remarkably poor in ACAT KO lesions (Fig. 4, A and C; and Fig. S2, A and B). IHC analysis of microglia showed a significant increase in the number of IBA1+ cells in
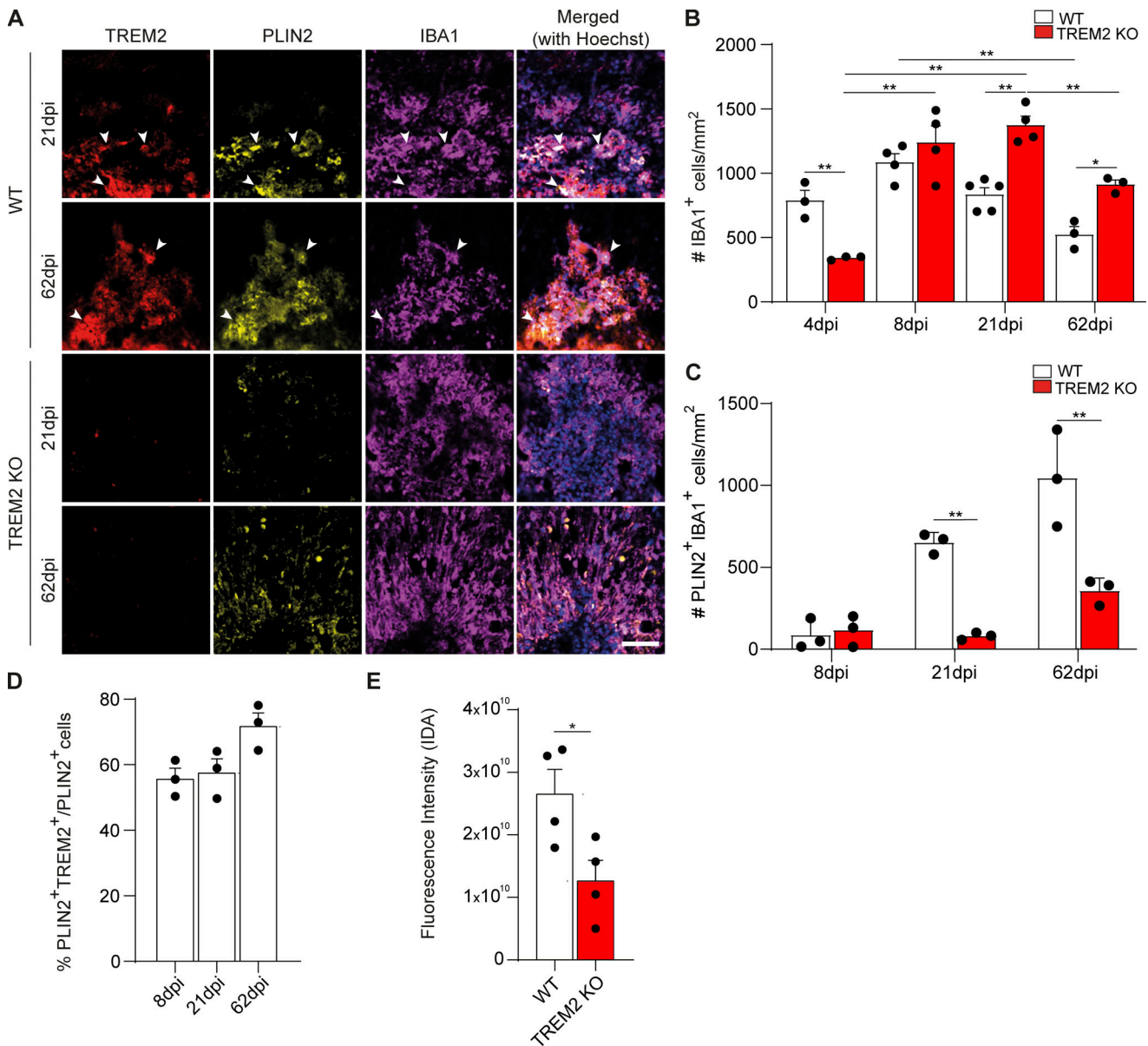
Figure 2. **TREM2 is required for innate immune cell resolution and foam cell formation. (A)** Confocal images of 21- and 62-dpi lesions from WT and TREM2 KO mice after staining for TREM2 (red), PLIN2 (yellow), and IBA1 (magenta), showing the colocalization of PLIN2 and TREM2 (arrowheads mark triple-positive cells). Scale bar, 50 μm. **(B)** Quantification of the density of IBA1+ cells at 4, 8, 21, and 62 dpi. **(C)** The density of PLIN2+IBA1+ microglia (cells per mm²) was quantified for WT and TREM2 KO. **(D)** Quantification of the percentage of PLIN2+IBA1+ cells, which are also positive for TREM2, in 21-dpi WT lesions. **(E)** Quantification of cholesterol crystal fluorescence by reflection confocal microscopy in WT and TREM2 KO lesions at 21 dpi. $n$ = 3–5 animals per condition for A–D; $n$ = 4 lesions per condition for E. Data represent mean ± SEM. For B and C, P values were calculated using two-way ANOVA (A) with Šidák post hoc correction. For D, P values were calculated using one-way ANOVA. For E, P values were calculated using two-tailed unpaired $t$ test. *, P < 0.05; **, P < 0.01. IDA, integrated density area.

lesions at 21 dpi (Fig. 4, D and E). While the number of GFAP+ astrocytes were unaltered, there was a slight reduction in the percentage of MAC2+/IBA1+ cells in ACAT KO lesions at 4 dpi (Fig. S2, C and D). The exacerbated innate immune inflammation at 21 dpi could not be explained by a defect in myelin degradation, as the percentage of myelin-loaded microglia (labeled with the lipid dye fluoromyelin [FM] and the lysosome-associated membrane glycoprotein 1 [LAMP1]) was not different in lesions of WT and ACAT KO mice (Fig. 4 F). Similar to TREM2 KO lesions, using reflection microscopy and TEM, we detected

fewer cholesterol crystals in microglia of ACAT KO lesions compared with WT (Fig. S2 E). Reflection microscopy of myelin-treated microglia confirmed that cholesterol crystals formed both in lysosomes and on lipid droplets (Fig. S2, F–H). Therefore, the phase transition of cholesterol into its crystalline form can likely initiate in lipid droplets. Indeed, occasionally very large crystals (>15 μm) were observed in the lesions by TEM (Fig. S2 I). Thus, our data show that the ability to esterify cholesterol is a key adaptive function of microglia and a necessary response for regeneration to occur.
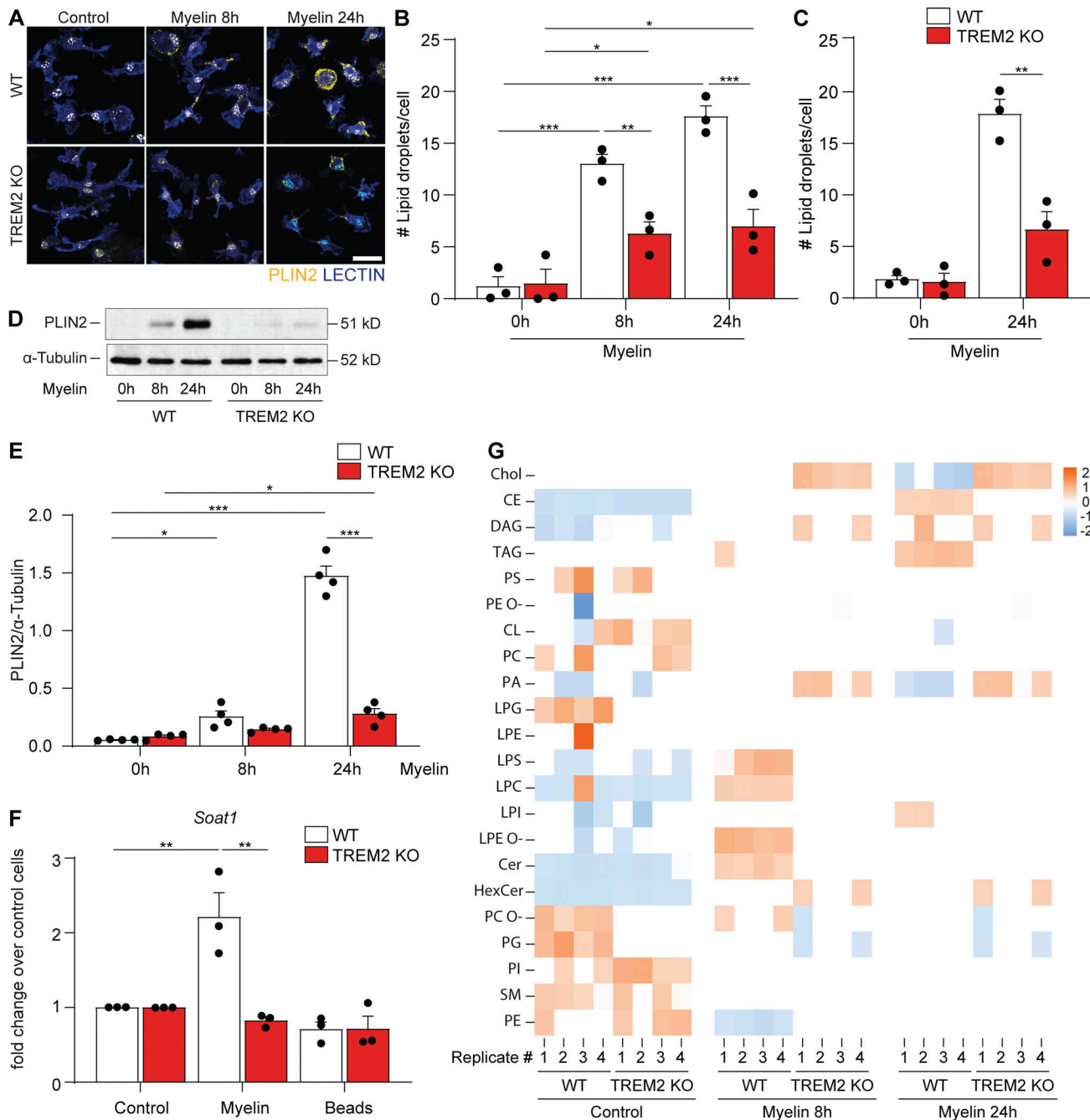
**Figure 3. Cholesterol esterification and lipid droplet formation are defective in myelin-treated TREM2 KO microglia. (A)** Confocal images of WT and TREM2 KO microglia of the control condition (0 h) or treated with myelin for 8 and 24 h and stained for PLIN2, isolectin (lectin), and Hoechst. Scale bar, 25 μm. **(B and C)** Quantification of the number of lipid droplets per cell in postnatal (B) and adult (C) microglia. **(D and E)** Western blots and quantification for PLIN2 and α-tubulin in WT and TREM2 KO cells in serum-free media 8 h and 24 h after myelin treatment. The intensity of the band of PLIN2 was normalized to α-tubulin. **(F)** Real-time PCR for ACAT (*Soat1*) in WT and TREM2 KO cells in serum-free media 24 h after myelin treatment and 24 h after exposure to beads. Data are expressed as fold change over the untreated cells. **(G)** Untargeted lipidomics analysis of WT and TREM2 KO cells cultured in serum-free media or with myelin for 8 or 24 h. $n = 3$ biological replicates per condition for A–C, and F; $n = 4$ biological replicates per condition for D and E; $n = 4$ biological replicates for F. The results are representative of three independent experiments. For the lipidomics analysis, each replicate was from a different animal. Data represent as mean ± SEM. P values were calculated using two-way ANOVA (A) with Šidák post hoc correction. *, $P < 0.05$; **, $P < 0.01$; ***, $P < 0.001$. CE, cholesterol ester; Chol, cholesterol.

## ER stress and protein synthesis defects in demyelinating lesions of TREM2-deficient mice

As cholesterol esterification and TAG biosynthesis take place in the ER, we speculated that activation of ER stress could represent the underlying reason for impaired lipid droplet formation in TREM2 KO microglia. Myelin debris uptake might lead to cholesterol overload in the ER, which is known to trigger the activation of the eukaryotic translation initiation factor 2-α
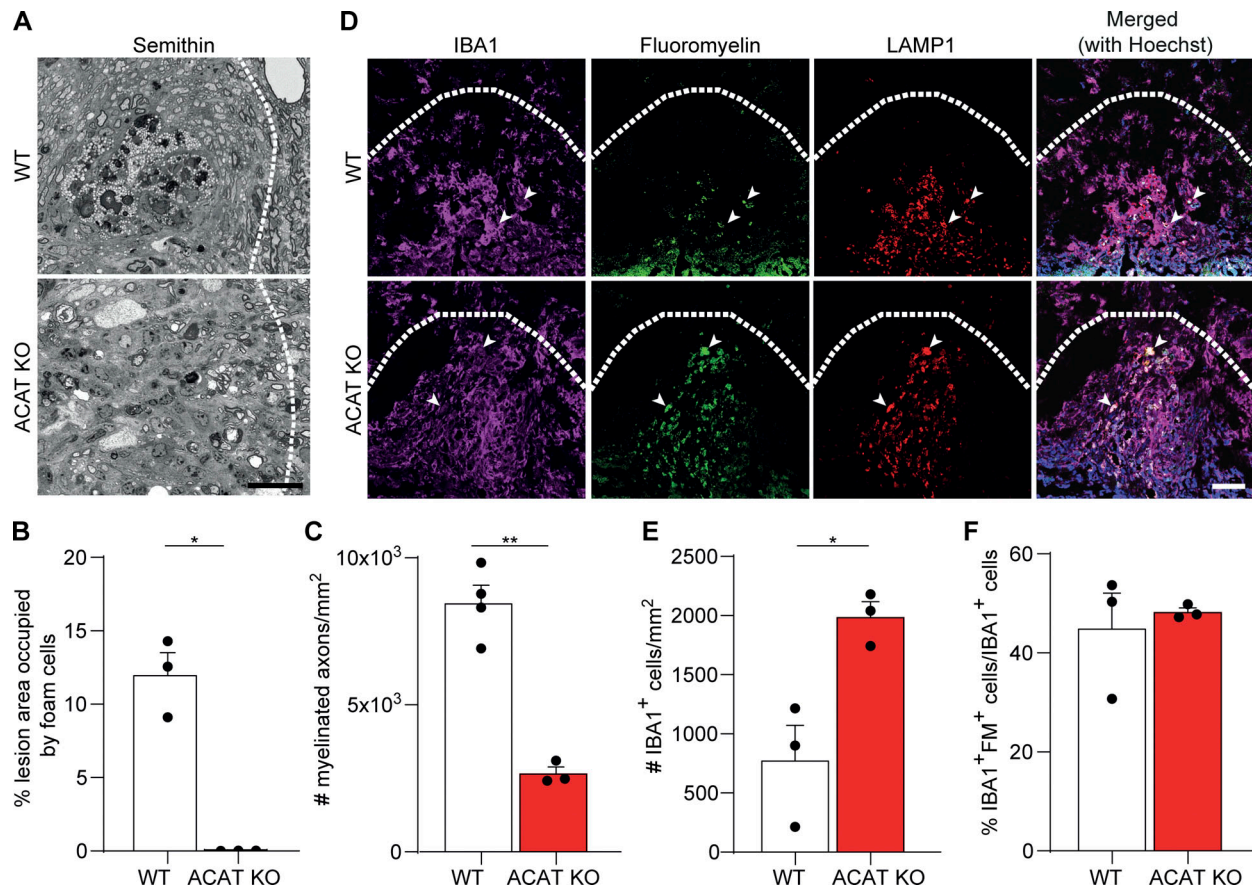
Gouna et al.
Lipid droplet biogenesis required for remyelination

Journal of Experimental Medicine    5 of 12
https://doi.org/10.1084/jem.20210227

**Figure 4. Cholesterol esterification is necessary for remyelination. (A)** Representative images of azure blue staining of semithin sections from 21-dpi lesions from WT and ACAT KO mice. **(B and C)** The quantification of foam cells (B) and remyelinated axons (C). **(D–F)** Confocal images (D) and quantification (E) of 21-dpi lesions showing increased density of inflammatory cells (IBA1+, magenta) in ACAT KO mice compared with the WT control. The number of phagocytes with undigested myelin (arrowheads in D labeled with IBA1, magenta; FM, green; and LAMP1, red) was similar between WT and ACAT KO animals; quantification shown in F. Scale bars, 15 μm in A and 50 μm in D. n = 3–4 mice per condition for all the experiments. Data represent mean ± SEM. P values were calculated using two-tailed unpaired t test. *, P < 0.05; **, P < 0.01.

kinase 3, which phosphorylates and inactivates eukaryotic translation initiation factor 2 α (eIF2α), attenuating protein translation. Indeed, IHC analyses of microglia in demyelinating lesions revealed an increase in the number of IBA1+ cells immunopositive for phosphorylated eIF2α (p-eIF2α) in TREM2 KO compared with WT lesions (Fig. 5, A and B). To determine the rate of protein translation, lesioned WT and TREM2 KO animals were injected with O-propargyl-puromycin (OP puro), which is incorporated into nascent polypeptide chains. TREM2 KO lesions showed a significant decrease in the number of OP puro+IBA1+ cells (Fig. 5, C and D), indicating a low rate of protein synthesis in TREM2 KO microglia. We hypothesized that myelin debris uptake–induced cellular stress might be the reason for defective protein translation in TREM2 KO microglia. To explore this possibility, we treated primary microglia with myelin debris and quantified the incorporation of OP puro. A strong increase in OP puro incorporation was observed after myelin treatment in both WT and TREM2 KO microglia (Fig. S3, A and B). However, the incorporation rapidly declined in TREM2 KO but not WT cells after 24 h of treatment, suggesting active suppression of protein synthesis in the absence of TREM2. In addition, we observed by Western blot analysis increased levels of p-eIF2α in

myelin-treated TREM2 KO compared with WT microglia, further supporting our conclusion that ER stress may turn off protein translation (Fig. S3, C and D). Furthermore, the levels of active, phospho-Jun N-terminal kinase (p-JNK) was also increased in TREM2 KO microglia, which is known to contribute to the phosphorylation and inactivation of eIF2α (Fig. S3, C and E).

Our data support the hypothesis that myelin debris uptake in TREM2 KO microglia results in ER stress and suppression of protein translation, which possibly impairs lipid droplet biogenesis. Thus, we tested whether mitigation of ER stress is able to improve lipid droplet biogenesis in TREM2 KO mice. We applied 4-phenyl butyric acid (PBA), a widely used small-molecule chaperone known to reduce ER stress (Ozcan et al., 2006), and found that pretreatment of microglia with PBA restored the formation of lipid droplets in TREM2 KO microglia after myelin treatment (Fig. S3, F and G). In addition, when TREM2 KO mice were treated with a daily injection of PBA, we observed an increase in lipid droplet formation in IBA+ cells in lesions at 21 dpi (Fig. 5, E and F). There was also a significant decrease of IBA1+ cells in TREM2 KO lesions at 21 dpi, providing evidence for a beneficial effect of PBA in inflammation resolution in lesions (Fig. 5, G and H). The amount of myelin debris (labeled with FM) in the lysosomes of microglia
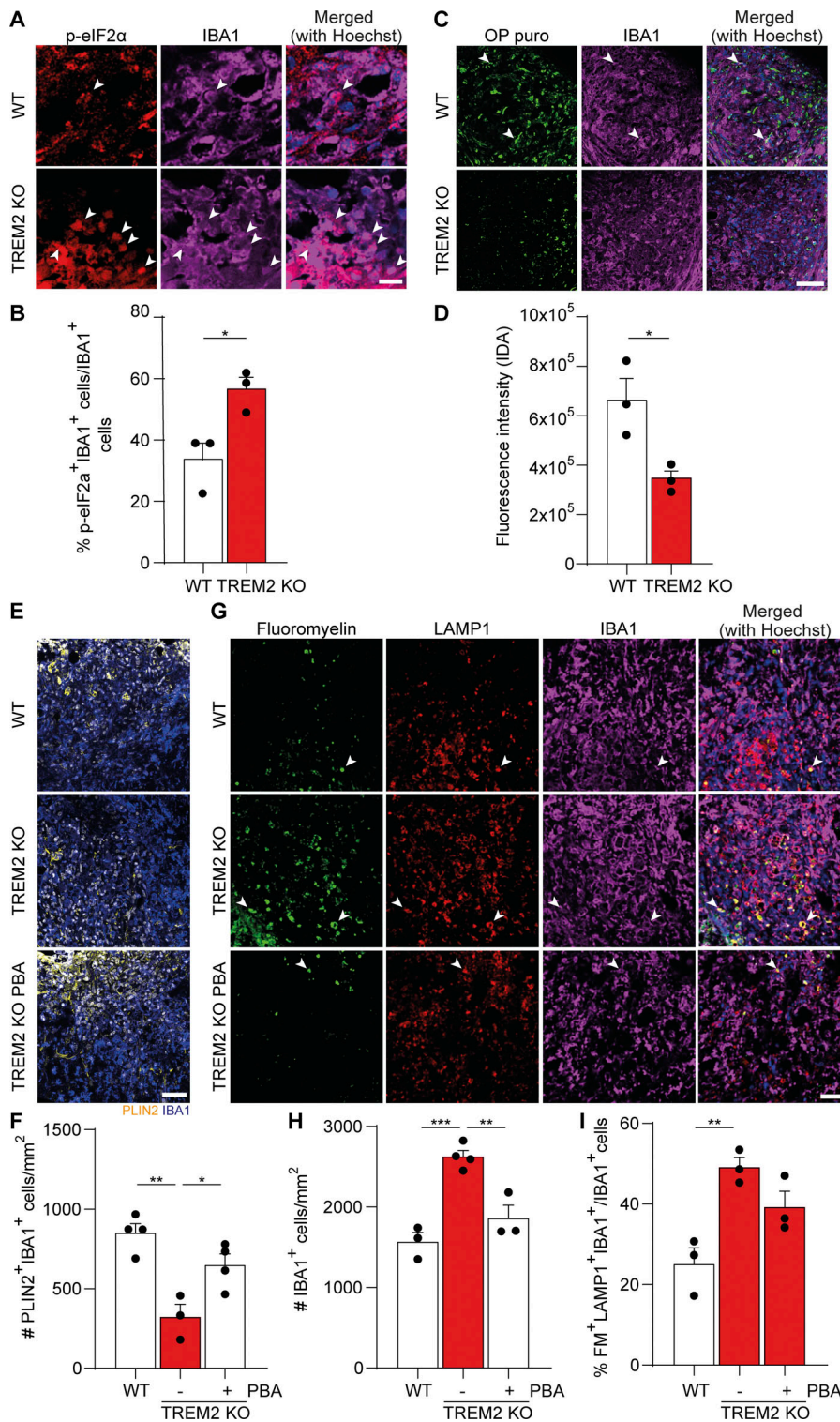
Figure 5. **ER stress and protein synthesis defects in TREM2 KO demyelinating lesions.** **(A and B)** Confocal images (A) and relative quantification (B) of 21-dpi lesions from WT and TREM2 KO mice after staining for p-eIF2α (red), IBA1 (magenta), and Hoechst (blue). **(C)** Confocal images of 21-dpi lesions from WT and TREM2 KO mice injected with OP puro (green) 1 h before perfusion and stained for IBA1 (magenta). **(D)** The rate of incorporation was quantified by measuring the integrated density area (IDA) of OP puro within the IBA1⁺ cells within the lesion borders. **(E)** Confocal images and quantification of 21-dpi lesions from WT and TREM2 KO and TREM2 KO mice treated with daily injection of 100 mg/kg PBA stained for PLIN2 (yellow), IBA1 (blue), and Hoechst (white). **(F)** Quantification of the density of PLIN2⁺IBA1⁺ cells. **(G)** Representative confocal images from WT, TREM2 KO, and PBA-treated TREM2 KO mice, stained for FM (green), LAMP1 (red), IBA1 (magenta), and Hoechst (blue); arrowheads mark the colocalization of the markers. **(H)** Quantification of the total number of IBA1⁺ microglia per mm² of lesion. **(I)** Percentage of FM⁺LAMP1⁺IBA1⁺ cells over the total number of IBA1⁺ cells within the lesion boundaries. Scale bars, 10 μm in A and 50 μm in C, E, and G. For all the experiments, n = 3–4 animals per condition. Data represent mean ± SEM. P values were calculated using two-tailed unpaired $t$ test for B and D and one-way ANOVA followed by Tukey's post hoc test for F, H, and I. *, $P < 0.05$; **, $P < 0.01$; ***, $P < 0.001$.

(labeled for LAMP1) did not differ in lesions of TREM2 KO mice (Fig. 5, G and I). Taken together, these results show that lipid-induced ER stress contributes to impaired lipid droplet formation in TREM2 KO mice.

## General discussion and conclusions
Demyelinating injury is followed by phagocytosis of cholesterol-rich myelin debris by microglia/macrophages. While lysosomal enzymes are responsible for the degradation of most myelin components, cholesterol cannot be degraded and is therefore transferred from late endosomes to the ER. Because the ER has an extremely low cholesterol carrying capacity, there are adaptive mechanisms that protect phagocytes from the toxic effect of free cholesterol (Moore and Tabas, 2011). One protective factor is the liver X receptor (LXR), which regulates the transcription of cholesterol export genes (Evans and

Mangelsdorf, 2014). Another is ACAT, which detoxifies cholesterol by forming cholesterol esters for storage in lipid droplets (Moore and Tabas, 2011). Here, we show that cholesterol esterification is necessary for phagocytes to adapt to excess cholesterol arising from phagocytosis of myelin debris in demyelinating lesions. When this buffering mechanism is defective, phagocytes do not resolve from demyelinating lesions, and the regenerative response fails. We found that TREM2-deficient mice are unable to elicit the adaptive response to excess cholesterol exposure. The reason could be that TREM2-dependent gene expression is necessary to trigger the generation of enzymes required for lipid droplet formation. Because TREM2-deficient phagocytes are able to internalize myelin debris but fail to mount the necessary metabolic responses to the internalized cargo, they become exposed to the toxicity of free cholesterol that builds up with time. Consequently, cholesterol-induced cellular stress develops. Previous studies have shown that cholesterol loading of macrophages activates the unfolded protein response pathway (Feng et al., 2003), and in accordance with these studies, we observed evidence of ER stress in myelin debris–loaded TREM2-deficient phagocytes. Transient protein synthesis inhibition is an important protective mechanism used by cells during ER stress (Xu et al., 2005; Lin and Popko, 2009); however, in the context of myelin debris clearance, such a response could be deleterious as it also blocks the synthesis of lipid metabolism genes. Our lipidomic analysis reveals that TREM2-deficient phagocytes not only fail to generate cholesterol esters but also are deficient in TAG generation. The accumulation of phosphatidic acid in TREM2-deficient phagocytes points to decreased activity of lipin phosphatidic acid phosphatase, which catalyzes the conversion of phosphatidic acid to diacylglycerol (DAG; Carman and Han, 2019). Lipin is unique among biosynthetic enzymes in TAG generation as its enzyme activity is regulated by its transition between the ER and the cytosol, a process under the control of mammalian target of rapamycin–mediated phosphorylation of lipin. Intriguingly, a previous study provided evidence of defective mammalian target of rapamycin signaling in TREM2-deficient microglia (Ulland et al., 2017), providing a possible link of how TREM2 may control TAG generation.

While we highlight a role of lipid droplets in buffering cholesterol-mediated toxicity, it is increasingly becoming clear that lipid droplets also provide protective functions against other forms of lipotoxicity. For example, elevated reactive oxygen species induces the formation of lipid droplets, which sequester polyunsaturated fatty acids, protecting them from oxidative damage (Ioannou et al., 2019). In another context, lipid droplets do not appear to be protective but, instead, are harmful in their role of mediating neuronal damage together with reactive oxygen species generated by defective mitochondria or inflammatory signals (Liu et al., 2015). It is interesting to compare our results with a recent study performed in a model of chronic demyelination, which shows that TREM2-deficient mice accumulate oxidized and nonoxidized cholesterol ester (Nugent et al., 2020). Whereas our results show that TREM2 function is required for the formation of cholesterol esters and lipid droplets, Nugent et al. (2020) came to a different conclusion.

The reasons for these discrepancies are not clear, but one possibility is that TREM2 has additional functions in models of chronic injury in which the generation of reactive oxygen species plays a more important role. Our experiments using ACAT-deficient mice show that remyelination fails when microglia/macrophages are unable to transition into foamy phagocytes. These results imply that the generation of lipid droplets represents an adaptive response required for efficient lesion recovery after acute demyelination. Such foamy phagocytes filled with lipid droplets accumulate in the resolution phase of lesions in aged mice, a condition associated with poor remyelination (Cantuti-Castelvetri et al., 2018; Grajchen et al., 2018). Although these findings superficially appear to contradict each other, it is important to recall that there are two major pathways to prevent the accumulation of free cholesterol in cells. In aging, the underlying deficit is the insufficient activation of LXR, a pathway required to induce the expression of genes involved in cholesterol efflux, such as the plasma membrane cholesterol transporters and apolipoprotein E (Cantuti-Castelvetri et al., 2018). Consequently, excessive amounts of cholesterol-rich myelin debris accumulate in phagocytes, resulting in increased formation of lipid droplets and the transition of cholesterol into crystals. This is in contrast to TREM2 deficiency, which is associated with impaired formation of lipid droplets followed by the exhaustion of phagocyte buffering capacity and stress pathway activation. It is interesting to note that cholesterol crystals were detected both on lipid droplets and in lysosomes. Whereas the overall number of crystals declines, crystals associated with lysosomes still form in TREM2-deficient microglia. Currently, we do not know which of the two types of crystals plays a pathogenic role, but it is tempting to speculate that crystals formed in lysosomes that can cause lysosomal rupture and inflammasome activation are more damaging.

In summary, the results presented here add to a developing picture of how phagocytes function in clearing excess cholesterol that is building up in lesions after a demyelinating insult. It appears that both cholesterol efflux and esterification are essential and that the activation of both pathways is required to promote the resolution of innate immune inflammation and to support remyelination.

## Materials and methods
### Mice, cell lines, and antibodies
#### Mice
WT C57BL/6 mice were purchased from Janvier Labs, kept in groups of three in Greenline IVC GM500 plastic cages, and housed in a temperature-controlled environment (21 ± 2°C) on a 12-h light/dark cycle with food and water available ad libitum in the animal facility in German Center for Neurodegenerative Diseases. Trem2−/− mice were established in the C57BL/6 background. SOAT1 KO mice were purchased from The Jackson Laboratory and were backcrossed once in the C57BL/6 background (#002896). All mice used for our experiments were male. All experiments were approved by the institutional animal use and care committee. For the in vivo treatment, 50 mg/kg PBA was administered i.p. every day, starting the day of the LLC injection.

## Cell line

L929 cells were grown in DMEM supplemented by 10% FCS, L-glutamine, and antibiotics. For maintenance, these cells were resuspended in freezing media containing 50% FCS and 10% DMSO at concentrations of $5 \times 10^6$ to $1 \times 10^7$ cells/ml. Aliquots in 1.5-ml cryotubes were frozen slowly at 1°C/min by placing tubes in a Nalgene cryo freezing container in a −80°C freezer and then transferring to liquid nitrogen storage.

## Primary antibodies

Rabbit IBA1 (234 004, 1:500 for IHC; Synaptic Systems), PLIN2 (GP40, 1:500 for histology, 1:3,000 for Western blotting; PRO-GEN), p-eIF2α (ab32157, 1:200 for staining, 1:2,000 for Western blotting; Abcam), total eIF2α (2103, 1:2,000 for Western blotting; Cell Signaling Technology), JNK1+JNK2 (p-T183+Y185, ab4821, 1:1,000 for Western blotting; Abcam), JNK1+JNK2 (ab112501, 1:1,000 for Western blotting; Abcam), LAMP1 (sc-19992, 1:100 for histology; Santa Cruz Biotechnology), TREM2 (AF1729, 1:200 for histology; R&D Systems), α-tubulin clone B-5-1-2 (T5168; Sigma-Aldrich); GAPDH (ab9484, 1:5,000 for Western blotting; Abcam), GFAP (173004, 1:500; Synaptic Systems), MAC2 (125402, 1:250; BioLegend), APC (OP80, 1:100; Merck Calbiochem), and oligodendrocyte transcription factor 2 (OLIG2; ab9610, 1:200; Millipore).

## Secondary antibodies

Alexa Fluor 488–, 647–, and 555–conjugated antibodies (Invitrogen) were used.

## Other reagents

FM green fluorescent myelin stain from Invitrogen (Cat. F34651), Hoechst 33342 from Sigma (Bisbenzimide Hoechst 33342, B2261), and isolectin from Vector Laboratories (DL-1208). L-α-LPC from egg yolk was from Sigma (L4129).

## Kits

The Click-iT Cell Reaction Buffer Kit was used (C10269; Thermo Fisher Scientific).

## IHC

Animals were anesthetized by 10 mg/ml ketamine and 1 mg/ml xylazine solution i.p. perfused transcardially with 4% paraformaldehyde (PFA). Postfixation of spinal cords was done in 4% PFA overnight. The brain tissue was further cryoprotected in 30% sucrose in PBS for 24 h. After freezing the tissue on dry ice using Tissue-Tek O.C.T., 16-μm coronal sections were cut by a Leica CM 1900 cryostat. The sections were rinsed with 1× PBS containing 0.2% Tween 20 and permeabilized in 0.5% Triton X-100 for 10–30 min depending on primary antibody. For the TREM2 staining, antigen retrieval was performed for 10 min at 120°C in the autoclave in sodium citrate buffer (10 mM, pH 6). Blocking solution (1% FBS, 1% fish gelatin, and 1% bovine calf serum in PBS) was added for 1 h at room temperature to block endogenous mouse tissue immunoglobulins. Primary antibodies, diluted in 10% blocking solution, were added and incubated overnight at 4°C. On the following day, sections were incubated with secondary antibodies, diluted in 10% blocking

solution, for 1 h at room temperature. The sections were washed with PBS followed by incubation in secondary antibody for 1 h at room temperature. Sections were then washed, stained with 2 μg/ml Hoechst 33342, and mounted with fluorescence mounting medium (81381; Sigma-Aldrich). For the protein synthesis analysis, cells were incubated with 10 μM OP puro (HY-15680; MedChemExpress) for 60 min. The cells were then fixed in 4% PFA. The cells were permeabilized in 0.1% Triton X-100 for 3 min, washed, and processed with the Click-iT Cell Reaction Buffer Kit (C10269; Thermo Fisher Scientific) according to the manufacturer's instructions. Briefly, the cells were incubated for 30 min with a solution of reaction buffer, $CuSO_4$, buffer additive, and 5 μM Alexa Fluor 488 Azide (A10266; Thermo Fisher Scientific). The cells were then washed and stained with isolectin. For the in vivo study, LLC lesions were induced as described above. 1 h before the perfusion, the animals were anaesthetized with medetomidine-midazolam-fentanyl (MMF), and a solution of 10 μM OP puro was administered via i.p. injection. The lesions were sectioned and stained with the Click-iT Cell Reaction Buffer Kit and for conventional histology. The cells were imaged with a Leica SP5 confocal microscope with a 63× objective. For reflection microscopy, 14-μm sections were stained with DyLight 594–conjugated GSL I-B4 isolectin (DL1207; Vector Laboratories) and DAPI. The sections were then imaged with a Leica SP5 AOBS confocal microscope according to the manufacturer's instructions. For the quantification of the crystals, at least two random 100× pictures per lesion were taken to calculate the integrated density area. For the quantification of the lesion area, the surface of demyelination shown by negative FM staining was measured in serial sections of a lesion, which were separated by a known distance. According to the truncated cone model, lesion volume was calculated in IPython. The code is available at https://github.com/lenkavaculciakova/lesion_volume.

## TEM

Mouse spinal cords were fixed in 2.5% glutaraldehyde and 4% PFA in 0.1 M sodium cacodylate buffer at pH 7.4 after deep anesthesia (isoflurane) perfusion. Spinal cords were vibratome sectioned and immersion fixed in the same buffer for 24 h at 4°C. After tissue trimming and washes in 0.1 M sodium cacodylate buffer, postfixation in reduced osmium (2% osmium, 2.5% potassium ferrocyanide in 0.1 M cacodylate buffer) was followed by en bloc uranyl acetate (1% aqueous uranyl acetate) contrasting, graded dehydration in ethanol, and embedding in epon resin (Serva). After ultrathin sectioning, the grids (Leica UC7 Ultramicrotome) were contrasted by 1% uranyl acetate and lead citrate (Ultrostain; Leica). Semithin sections were contrasted by an equimolar mixture containing 1% methylene blue (Carl Roth GmbH & Co. Kg) in 100 ml sodium tetraborat and 1% (1 g) azure Blue (Carl Roth) in 100 ml water. Images were acquired with a JEOL JEM 1400plus TEM equipped with a Ruby 8 megapixel CCD camera. For each analysis, randomly selected regions in three to five different animals were imaged. Data analysis was performed using ImageJ 1.41 software (https://imagej.net/Fiji). The g-ratios were measured with ImageJ on transverse electron micrographs at 8,000× magnification. The perimeters of each axon and the myelin sheath were measured with the freehand

tool by tracing the outer surfaces of each structure. The g-ratio was calculated as the diameter of the axon over the diameter of its myelin.

## Myelin isolation and purification

Myelin was isolated from 8-wk-old C57BL/6 mouse brains by sequential centrifugation on discontinuous sucrose gradient according to a protocol previously described (Norton and Poduslo, 1973), with some modifications. The ultracentrifugation was done using an SW41 Ti rotor. The brain tissues were homogenized with a Dounce homogenizer in a solution containing 10 mM Hepes, 5 mM EDTA, and 0.32 M sucrose. The homogenized tissue was layered on Hepes/EDTA buffer containing 0.85 M sucrose and centrifuged at 24,600 rpm for 30 min with low deceleration and acceleration. The crude myelin fraction was removed from the interface, resuspended in ice-cold distilled water, and centrifuged at 9,500 rpm for 15 min. The hypo-osmotic shock was applied to the pellet two more times. The pellet from the last step was dissolved in Hepes/EDTA buffer containing 0.3 M sucrose and placed over the 0.85 M sucrose; all the centrifugation steps and hypo-osmotic shocks were repeated as before. Eventually, the purified myelin pellet was resuspended in 1 ml PBS and stored at –20°C.

## Microglia treatment

Microglia were isolated from C57BL/6, P6-P8 WT mice by MACS technology. Brain tissue was dissociated using a Papain-based Neural Tissue Dissociation Kit (Miltenyi Biotec). Briefly, brain tissue was removed, cut into small pieces, and dissociated by enzymatic digestion provided in the kit. The tissue suspension was applied to a 70-μm cell strainer and washed twice with DMEM containing 1 mM sodium pyruvate. The final pellet was resuspended in 10 vol of DMEM containing 10% FCS, 1 mM sodium pyruvate, and 1% antibiotics (DMEM/FCS) plus 1 vol CD11b microbeads (130-093-634; Miltenyi Biotec) and incubated at 4°C for 15 min. After washing with DMEM/FCS, the pellet was resuspended in 500 μl of the same medium and applied to a MACS column in the magnetic field after washing three times; the CD11b^{+} cells (microglia) were flushed out of the column and centrifuged at 400 ×g for 10 min at 4°C. Isolated microglia were plated on 8-mm coverslips at $7 \times 10^4$ cell/ml and incubated until confluent. Myelin was sonicated in an ultrasound water bath for 5 min. Primary microglia cultures were treated with 8 μg myelin and incubated for 2–24 h. The cells were then fixed with 4% PFA and stained for PLIN2, DyLight 694–labeled tomato lectin, and 2 μg/ml Hoechst 33342. The cells were imaged on a Leica SP5 confocal microscope with a 63× objective.

## LLC-induced demyelination

Stereotactic injection of LLC in the spinal cord was performed in WT C57BL/6, SOAT1, and TREM2 mice that were 9–15 wk old. 1% LLC was prepared by dissolving L-α-LPC from egg yolk (L4129; Sigma) in PBS, pH 7.4 (10010056; Gibco). 3% Monastral Blue was prepared by dissolving Copper(II) phthalocyanine-tetrasulfonic acid tetrasodium salt (274011; Sigma-Aldrich) in Milli-Q water, and the solution was sterilized by filtration through a 0.45-μm filter and autoclaving. Prior to injection, 1 μl 3% Monastral Blue

was mixed with 25 μl 1% LLC. Glass Capillaries for Nanoliter 2010 (504949 or 4878; World Precision Instruments) were pulled using the P-1000 Next Generation Micropipette Puller (Sutter Instrument). The program had the following parameters: heat, 530; pull, 0; velocity 60; time, 250; pressure, 500; ramp, 520; microinjection–BF100.50.10; tip, <1 μm; taper, 6–8 mm; R, ~40–80 MΩ; heat = ramp; FB255B; and 2.5-mm box. Before surgery, the animals were anesthetized by MMF i.p. (0.5 mg/kg body weight medetomidine, 5.0 mg/kg midazolam, and 0.05 mg/kg fentanyl). The anesthetized animals were kept on a heating pad at 37°C, and the anesthetic depth was monitored by checking the reflex between the toes and the corneal reflex. The surgery and intraspinal injection of LLC was conducted using the Digital Mouse Stereotaxic Frame and Nanoliter 2010 injector with MICRO4 controller (World Precision Instruments) as previously described (Cantuti-Castelvetri et al., 2018). After the spinal cord was exposed, the capillary was positioned 0.55 mm lateral to the dorsal artery and lowered 1.20 mm into the tissue. At each injection site, 1 μl of 1% LLC containing 0.12% Monastral Blue was injected at a speed of 350 nl/min. 1 min after the end of the delivery, the capillary was retracted. After injection, the wound was sutured. After the operation, the animals were injected with 250 μl of 0.9% NaCl (normal saline solution) to compensate for the loss of blood and with the analgesic buprenorphine at a dose of 0.1 mg/kg. When MMF was used for anesthesia, 2.5 mg/kg atipamezole, 0.5 mg/kg flumazenil, and 1.2 mg/kg naloxone i.p. was administered to antagonize the anesthesia and awaken the animal. The animals were administered buprenorphine s.c. for 2 days after surgery.

## Gene expression analysis

For the isolation of RNA, primary microglia were treated with myelin or Fluoresbrite beads. At the end of the treatment, the cells were collected in Buffer RLT, and the RNA was isolated with RNeasy (74104; Qiagen). The RNA was retrotranscribed to cDNA with the Superscript III kit (18080051; Thermo Fisher Scientific). For quantitative PCR, the cDNA was quantified with the Power SYBR Green PCR Master Mix (4367659; Thermo Fisher Scientific) on an Applied Biosystems 7500 Fast Cycler according to the PCR mix data sheet. The relative quantification of each gene was performed with the $^{\Delta\Delta}$Ct method: Each gene was quantified, and its expression was normalized to the housekeeper gene cytochrome C1 (CYC1). The primers used for the analysis were SOAT1, forward 5′-TGCTGACGTCTTCCTGTGTC-3′; SOAT1 reverse WT, 5′-GAGCTGTTGGGGAGTAGGTG-3′; SOAT1 reverse mutant, 5′-CCTTCTATCGCCTTCTTGACG-3′; CYC1 forward, 5′-ATGGGGAGA TGTTCATGCGG-3′; and CYC1 reverse, 5′-CTGAGGTCAGGGGGT AAAGC-3′.

## Flow cytometry

The mice were anesthetized and perfused with cold PBS. Each brain was removed, and the lesions were microdissected individually under a dissection microscope. Dissociation of single cells was performed by using gentleMACS Dissociator with the Papain-based Neural Tissue Dissociation Kit (Miltenyi Biotec). Cell pellets were blocked with mouse FcR-blocking reagent (1:100, CD16/CD32 monoclonal antibody; eBioscience) and

stained for 15 min using 7-AAD (25 µg/ml; Thermo Fisher Scientific) and the antibodies against CD45 (1:200, eFluor450, 30-F11; eBioscience) and CD11b (1:200, PE/Cy7, M1/70; eBioscience) followed by washing with PBS. FACS analysis was performed with flow cytometry (SH800; Sony). Flow cytometry data were analyzed using FlowJo v10.

## Western blotting
Following separation with SDS-PAGE, the proteins were transferred from the gel onto the nitrocellulose membrane using the Mini Trans-Blot Module. The gel sandwich in blotting cassette was placed in the tank of the module containing transfer buffer (0.25 M Tris base, 1.92 M glycine, 20% methanol) with 100 V for 1 h. The membrane was washed in PBS with 0.1% Tween 20 (PBST) for 10 min, immersed in 3% BSA in PBST as a blocking solution for 30 min at room temperature, and then incubated with primary antibody in PBST at 4°C overnight. After washing, it was incubated with HRP-conjugated secondary antibody in PBST for 1 h at room temperature. Then targeted protein was detected with enhanced chemiluminescence method using Luminol enhancer and peroxide solutions (Pierce/Thermo Fisher Scientific) and visualized with an Odyssey Fc imager from LI-COR.

## Image processing and analysis
Images were acquired via a Leica TCS SP5 confocal microscope and processed and analyzed with Imaris (64×, version 9.2.0) and ImageJ 1.41 image processing software.

## Lipid extraction for mass spectrometry lipidomics
Mass spectrometry (MS)–based lipid analysis was performed by Lipotype GmbH as described elsewhere (Fitzner et al., 2020). Lipids were extracted using a two-step chloroform/methanol procedure (Ejsing et al., 2009). Samples were spiked with internal lipid standard mixture containing cardiolipin (CL) 16:1/15:0/15:0/15:0, ceramide (Cer) 18:1;2/17:0, DAG 17:0/17:0, hexosylceramide (HexCer) 18:1;2/12:0, lysophosphatidate (LPA) 17:0, LPC 12:0, LPE 17:1, lysophosphatidylglycerol (LPG) 17:1, lysophosphatidylinositol (LPI) 17:1, LPS 17:1, phosphatidate (PA) 17:0/17:0, phosphatidylcholine (PC) 17:0/17:0, phosphatidylethanolamine (PE) 17:0/17:0, phosphatidylglycerol (PG) 17:0/17:0, phosphatidylinositol (PI) 16:0/16:0, phosphatidylserine (PS) 17:0/17:0, cholesterol ester 20:0, sphingomyelin (SM) 18:1;2/12:0;0, TAG 17:0/17:0/17:0, and cholesterol D6. After extraction, the organic phase was transferred to an infusion plate and dried in a speed vacuum concentrator. First-step dry extract was resuspended in 7.5 mM ammonium acetate in chloroform:methanol:propanol (1:2:4 vol:vol:vol), and second-step dry extract was resuspended in 33% ethanol solution of methylamine:chloroform:methanol (0.003:5:1 vol:vol:vol). All liquid-handling steps were performed using Hamilton Robotics STARlet robotic platform with the Anti Droplet Control feature for organic solvents pipetting.

## MS data acquisition and analysis
Samples were analyzed by direct infusion on a Q Exactive Mass Spectrometer (Thermo Fisher Scientific) equipped with a TriVersa NanoMate ion source (Advion Biosciences). Samples were analyzed in both positive and negative ion modes with a resolution of $R_{m/z = 200}$ of 280,000 for MS and $R_{m/z = 200}$ of 17,500 for tandem MS experiments in a single acquisition. Tandem MS was triggered by an inclusion list encompassing corresponding MS mass ranges scanned in one-dimensional increments. Both MS and tandem MS data were combined to monitor cholesterol ester, DAG, and TAG ions as ammonium adducts; PC and PC O- as acetate adducts; and CL, PA, PE, PE O-, PG, PI, and PS as deprotonated anions. MS only was used to monitor LPA, LPE, LPE O-, LPI, and LPS as deprotonated anions; Cer, HexCer, SM, LPC, and LPC O- as acetate adducts, and cholesterol as ammonium adduct of an acetylated derivative. Data were analyzed with in-house–developed lipid identification software based on LipidXplorer (Herzog et al., 2011). Data postprocessing and normalization were performed using an in-house–developed data management system. Only lipid identifications with a signal-to-noise ratio >5 and a signal intensity fivefold higher than in corresponding blank samples were considered for further data analysis

## Statistics
Statistical analysis was performed with GraphPad Prism (GraphPad Software Inc.). The number of animals and cultures used for the experiments are indicated in the bars graphs of the figures or in the figure legends. No statistical methods were used to predetermine sample sizes, but our sample sizes are similar to those generally employed in the field. Data distribution was assumed to be normal, but this was not formally tested. To compare two groups, two-tailed unpaired Student's $t$ test was applied. One-way ANOVA followed by Tukey's post hoc test was performed for comparison of more than two groups. To compare the interactions between different animal or cell lines, two-way ANOVA followed by Tukey's post hoc test was used. A P value of <0.05 was considered significant in all tests. All values are represented as mean ± SEM.

## Online supplemental material
Fig. S1 depicts how myelin clearance and remyelination is impaired in TREM2 KO lesions. Fig. S2 displays how inflammation, remyelination, and cholesterol crystal formation is affected by the defective cholesterol esterification in the ACAT KO mouse model. Fig. S3 shows that in TREM2 KO microglia, ER stress is caused by myelin phagocytosis.

# References

Berghoff, S.A., L. Spieth, T. Sun, L. Hosang, L. Schlaphoff, C. Depp, T. Düking, J. Winchenbach, J. Neuber, D. Ewers, et al. 2021. Microglia facilitate repair of demyelinated lesions via post-squalene sterol synthesis. *Nat. Neurosci.* 24:47–60. https://doi.org/10.1038/s41593-020-00757-6

Bogie, J.F.J., E. Grajchen, E. Wouters, A.G. Corrales, T. Dierckx, S. Vanherle, J. Mailleux, P. Gervois, E. Wolfs, J. Dehairs, et al. 2020. Stearoyl-CoA desaturase-1 impairs the reparative properties of macrophages and microglia in the brain. *J. Exp. Med.* 217:e20191660. https://doi.org/10.1084/jem.20191660

Bosch-Queralt, M., L. Cantuti-Castelvetri, A. Damkou, M. Schifferer, K. Schlepckow, I. Alexopoulos, D. Lütjohann, C. Klose, L. Vaculčiaková, T. Masuda, et al. 2021. Diet-dependent regulation of TGFβ impairs reparative innate immune responses after demyelination. *Nat. Metab.* 3: 211–227. https://doi.org/10.1038/s42255-021-00341-7

Cantoni, C., B. Bollman, D. Licastro, M. Xie, R. Mikesell, R. Schmidt, C.M. Yuede, D. Galimberti, G. Olivecrona, R.S. Klein, et al. 2015. TREM2 regulates microglial cell activation in response to demyelination in vivo. *Acta Neuropathol.* 129:429–447. https://doi.org/10.1007/s00401-015-1388-1

Cantuti-Castelvetri, L., D. Fitzner, M. Bosch-Queralt, M.T. Weil, M. Su, P. Sen, T. Ruhwedel, M. Mitkovski, G. Trendelenburg, D. Lütjohann, et al. 2018. Defective cholesterol clearance limits remyelination in the aged central nervous system. *Science.* 359:684–688. https://doi.org/10.1126/science.aan4183

Carman, G.M., and G.S. Han. 2019. Fat-regulating phosphatidic acid phosphatase: a review of its roles and regulation in lipid homeostasis. *J. Lipid Res.* 60:2–6. https://doi.org/10.1194/jlr.S087452

Cunha, M.I., M. Su, L. Cantuti-Castelvetri, S.A. Müller, M. Schifferer, M. Djannatian, I. Alexopoulos, F. van der Meer, A. Winkler, T.J. van Ham, et al. 2020. Pro-inflammatory activation following demyelination is required for myelin clearance and oligodendrogenesis. *J. Exp. Med.* 217: e20191390. https://doi.org/10.1084/jem.20191390

Deczkowska, A., H. Keren-Shaul, A. Weiner, M. Colonna, M. Schwartz, and I. Amit. 2018. Disease-associated microglia: A universal immune sensor of neurodegeneration. *Cell.* 173:1073–1081. https://doi.org/10.1016/j.cell.2018.05.003

Dendrou, C.A., L. Fugger, and M.A. Friese. 2015. Immunopathology of multiple sclerosis. *Nat. Rev. Immunol.* 15:545–558. https://doi.org/10.1038/nri3871

Ejsing, C.S., J.L. Sampaio, V. Surendranath, E. Duchoslav, K. Ekroos, R.W. Klemm, K. Simons, and A. Shevchenko. 2009. Global analysis of the yeast lipidome by quantitative shotgun mass spectrometry. *Proc. Natl. Acad. Sci. USA.* 106:2136–2141. https://doi.org/10.1073/pnas.0811700106

Evans, R.M., and D.J. Mangelsdorf. 2014. Nuclear receptors, RXR, and the big bang. *Cell.* 157:255–266. https://doi.org/10.1016/j.cell.2014.03.012

Feng, B., P.M. Yao, Y. Li, C.M. Devlin, D. Zhang, H.P. Harding, M. Sweeney, J.X. Rong, G. Kuriakose, E.A. Fisher, et al. 2003. The endoplasmic reticulum is the site of cholesterol-induced cytotoxicity in macrophages. *Nat. Cell Biol.* 5:781–792. https://doi.org/10.1038/ncb1035

Fitzner, D., J.M. Bader, H. Penkert, C.G. Bergner, M. Su, M.T. Weil, M.A. Surma, M. Mann, C. Klose, and M. Simons. 2020. Cell-type- and brain-region-resolved mouse brain lipidome. *Cell Rep.* 32:108132. https://doi.org/10.1016/j.celrep.2020.108132

Franklin, R.J.M., and C. Ffrench-Constant. 2017. Regenerating CNS myelin - from mechanisms to experimental medicines. *Nat. Rev. Neurosci.* 18: 753–769. https://doi.org/10.1038/nrn.2017.136

Grajchen, E., J.J.A. Hendriks, and J.F.J. Bogie. 2018. The physiology of foamy phagocytes in multiple sclerosis. *Acta Neuropathol. Commun.* 6:124. https://doi.org/10.1186/s40478-018-0628-8

Herzog, R., D. Schwudke, K. Schuhmann, J.L. Sampaio, S.R. Bornstein, M. Schroeder, and A. Shevchenko. 2011. A novel informatics concept for high-throughput shotgun lipidomics based on the molecular fragmentation query language. *Genome Biol.* 12:R8. https://doi.org/10.1186/gb-2011-12-1-r8

Ioannou, M.S., J. Jackson, S.H. Sheu, C.L. Chang, A.V. Weigel, H. Liu, H.A. Pasolli, C.S. Xu, S. Pang, D. Matthies, et al. 2019. Neuron-astrocyte metabolic coupling protects against activity-induced fatty acid toxicity. *Cell.* 177:1522–1535.e14. https://doi.org/10.1016/j.cell.2019.04.001

Kotter, M.R., W.W. Li, C. Zhao, and R.J. Franklin. 2006. Myelin impairs CNS remyelination by inhibiting oligodendrocyte precursor cell differentiation. *J. Neurosci.* 26:328–332. https://doi.org/10.1523/JNEUROSCI.2615-05.2006

Lampron, A., A. Larochelle, N. Laflamme, P. Préfontaine, M.M. Plante, M.G. Sánchez, V.W. Yong, P.K. Stys, M.E. Tremblay, and S. Rivest. 2015. Inefficient clearance of myelin debris by microglia impairs remyelinating processes. *J. Exp. Med.* 212:481–495. https://doi.org/10.1084/jem.20141656

Lewcock, J.W., K. Schlepckow, G. Di Paolo, S. Tahirovic, K.M. Monroe, and C. Haass. 2020. Emerging microglia biology defines novel therapeutic approaches for Alzheimer's disease. *Neuron.* 108:801–821. https://doi.org/10.1016/j.neuron.2020.09.029

Lin, W., and B. Popko. 2009. Endoplasmic reticulum stress in disorders of myelinating cells. *Nat. Neurosci.* 12:379–385. https://doi.org/10.1038/nn.2273

Liu, L., K. Zhang, H. Sandoval, S. Yamamoto, M. Jaiswal, E. Sanz, Z. Li, J. Hui, B.H. Graham, A. Quintana, and H.J. Bellen. 2015. Glial lipid droplets and ROS induced by mitochondrial defects promote neurodegeneration. *Cell.* 160:177–190. https://doi.org/10.1016/j.cell.2014.12.019

Lloyd, A.F., and V.E. Miron. 2019. The pro-remyelination properties of microglia in the central nervous system. *Nat. Rev. Neurol.* 15:447–458. https://doi.org/10.1038/s41582-019-0184-2

Miron, V.E., A. Boyd, J.W. Zhao, T.J. Yuen, J.M. Ruckh, J.L. Shadrach, P. van Wijngaarden, A.J. Wagers, A. Williams, R.J.M. Franklin, and C. Ffrench-Constant. 2013. M2 microglia and macrophages drive oligodendrocyte differentiation during CNS remyelination. *Nat. Neurosci.* 16:1211–1218. https://doi.org/10.1038/nn.3469

Moore, K.J., and I. Tabas. 2011. Macrophages in the pathogenesis of atherosclerosis. *Cell.* 145:341–355. https://doi.org/10.1016/j.cell.2011.04.005

Norton, W.T., and S.E. Poduslo. 1973. Myelination in rat brain: method of myelin isolation. *J. Neurochem.* 21:749–757. https://doi.org/10.1111/j.1471-4159.1973.tb07519.x

Nugent, A.A., K. Lin, B. van Lengerich, S. Lianoglou, L. Przybyla, S.S. Davis, C. Llapashtica, J. Wang, D.J. Kim, D. Xia, et al. 2020. TREM2 regulates microglial cholesterol metabolism upon chronic phagocytic challenge. *Neuron.* 105:837–854.e9. https://doi.org/10.1016/j.neuron.2019.12.007

Ozcan, U., E. Yilmaz, L. Ozcan, M. Furuhashi, E. Vaillancourt, R.O. Smith, C.Z. Görgün, and G.S. Hotamisligil. 2006. Chemical chaperones reduce ER stress and restore glucose homeostasis in a mouse model of type 2 diabetes. *Science.* 313:1137–1140. https://doi.org/10.1126/science.1128294

Plemel, J.R., W.Q. Liu, and V.W. Yong. 2017. Remyelination therapies: a new direction and challenge in multiple sclerosis. *Nat. Rev. Drug Discov.* 16: 617–634. https://doi.org/10.1038/nrd.2017.115

Poliani, P.L., Y. Wang, E. Fontana, M.L. Robinette, Y. Yamanishi, S. Gilfillan, and M. Colonna. 2015. TREM2 sustains microglial expansion during aging and response to demyelination. *J. Clin. Invest.* 125:2161–2170. https://doi.org/10.1172/JCI77983

Reich, D.S., C.F. Lucchinetti, and P.A. Calabresi. 2018. Multiple Sclerosis. *N. Engl. J. Med.* 378:169–180. https://doi.org/10.1056/NEJMra1401483

Ulland, T.K., W.M. Song, S.C. Huang, J.D. Ulrich, A. Sergushichev, W.L. Beatty, A.A. Loboda, Y. Zhou, N.J. Cairns, A. Kambal, et al. 2017. TREM2 maintains microglial metabolic fitness in Alzheimer's disease. *Cell.* 170: 649–663.e13. https://doi.org/10.1016/j.cell.2017.07.023

Walther, T.C., J. Chung, and R.V. Farese Jr. 2017. Lipid droplet biogenesis. *Annu. Rev. Cell Dev. Biol.* 33:491–510. https://doi.org/10.1146/annurev-cellbio-100616-060608

Xu, C., B. Bailly-Maitre, and J.C. Reed. 2005. Endoplasmic reticulum stress: cell life and death decisions. *J. Clin. Invest.* 115:2656–2664. https://doi.org/10.1172/JCI26373

Gouna et al.
Lipid droplet biogenesis required for remyelination

Journal of Experimental Medicine
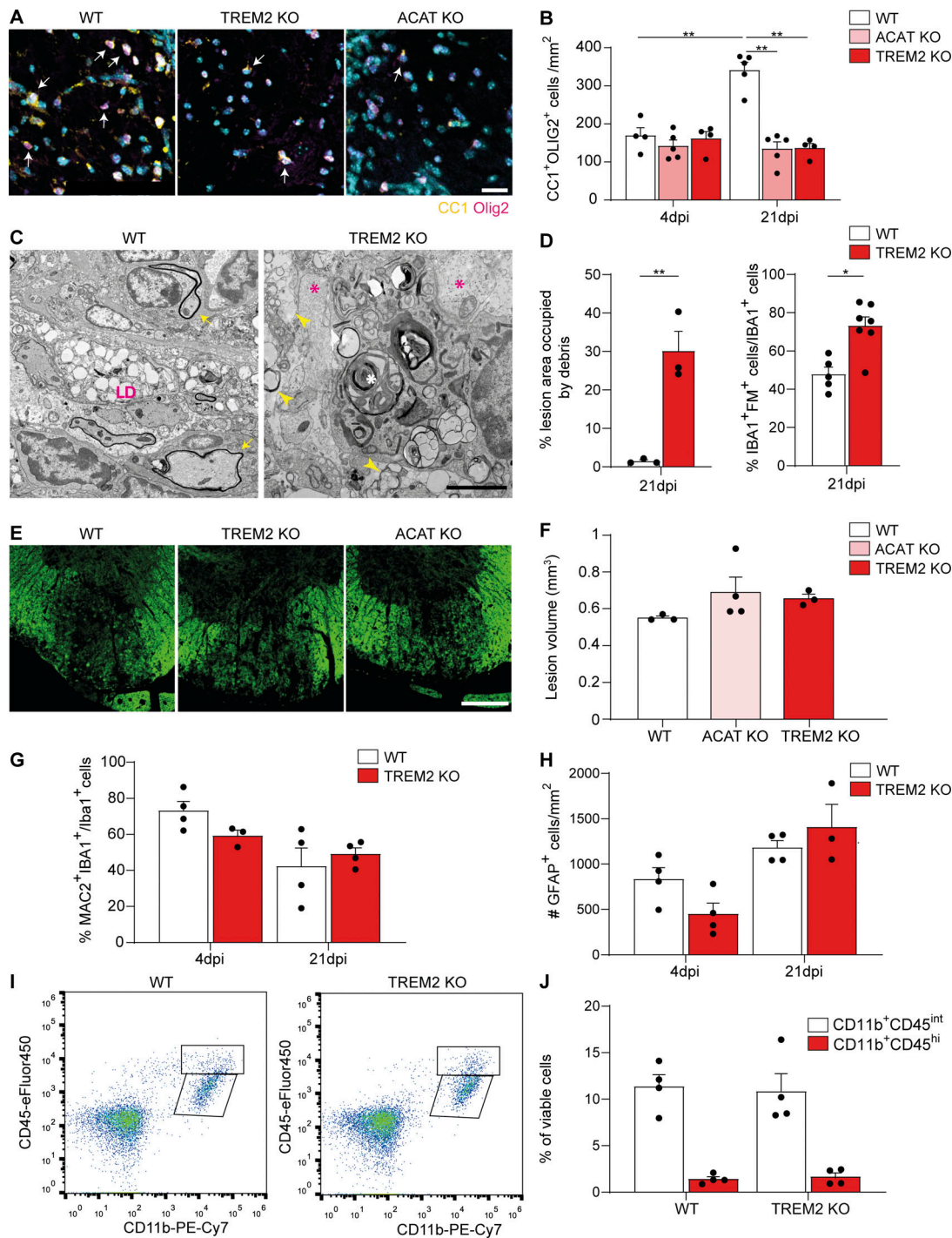https://doi.org/10.1084/jem.20210227

12 of 12

Figure S1. **Defective remyelination and myelin clearance in TREM2 KO lesions. (A)** Representative images of mature oligodendrocytes labeled for APC (clone CC1, yellow) and OLIG2 (magenta). **(B)** Relative quantification of the cell density. **(C)** TEM of WT and TREM2 KO lesions at 21 dpi, showing extracellular and intracellular debris (yellow arrowheads and white asterisk, respectively) in TREM2 KO phagocytes. Lipid droplets (LD) are observed in WT but not in TREM2 KO phagocytes. Remyelinated axons are detected in WT lesions (yellow arrows), while TREM2 KO lesions show naked axons (magenta asterisks). **(D)** Quantification of the accumulation of extracellular debris expressed as percentage of the lesion occupied by honeycomb-like debris and percentage of the IBA1+ cells, which contain debris (labeled by FM) in 21-dpi lesions of WT and TREM2 KO mice. **(E and F)** Representative images of 4-dpi lesions from WT, TREM2 KO, and ACAT KO mice and relative quantification of the lesion volume. **(G)** Percentage of IBA1+ cells, which are also MAC2+ in 4- and 21-dpi lesions of WT and TREM2 KO mice. **(H)** Quantification of the density of astrocytes (labeled for GFAP) in 4- and 21-dpi lesions of WT and TREM2 KO mice. **(I and J)** FACS plot showing the distribution of the brain mononuclear–phagocyte populations stained by CD11b (x axis) and CD45 (y axis) in 4-dpi lesions of WT and TREM2 KO mice and relative quantification. Populations of CD11b−CD45int microglia and CD11b+CD45hi CNS-associated macrophages were gated from viable cells. $n = 3–5$ animals per condition for all the depicted experiments. Scale bars, 10 µm in A, 2 µm in B, and 250 µm in E. Data represent mean ± SEM. P values were calculated with two-way ANOVA followed by Tukey's post hoc test for B, G, and H; with two-tailed unpaired t test for D and J; and with one-way ANOVA followed by Tukey's post hoc test for F. *, $P < 0.05$; **, $P < 0.01$.

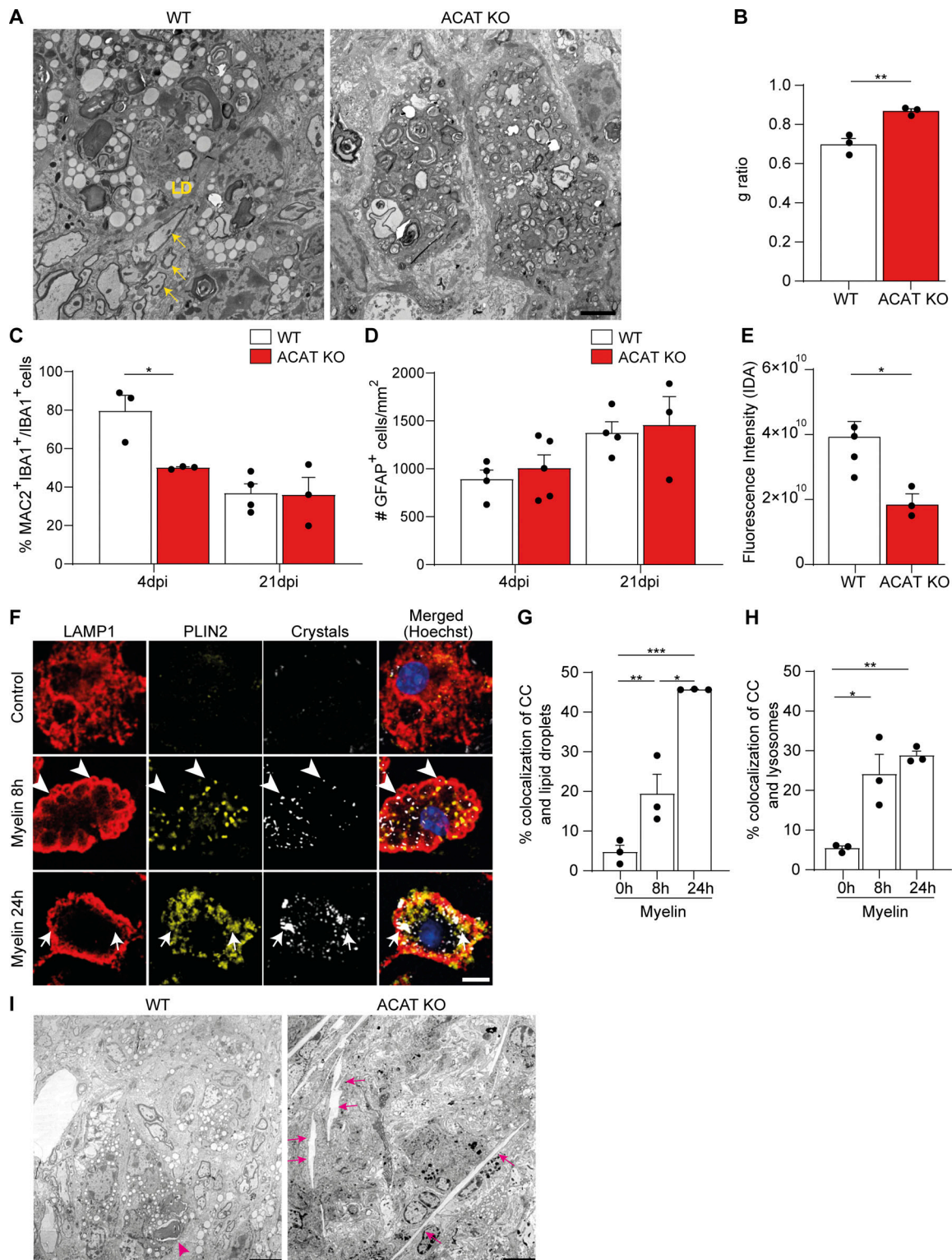**Figure S2. Defective cholesterol esterification affects remyelination, inflammation, and cholesterol crystal formation. (A)** TEM of 21-dpi lesions of WT and ACAT KO mice showing lipid droplets and remyelinated axons (yellow arrows) in WT but not in KO cells. **(B)** The g-ratio calculations of 21-dpi lesions of WT and ACAT KO mice. **(C and D)** Percentage of IBA1+ cells, which are also MAC2+, and quantification of the density of astrocytes (labeled for GFAP) in 4- and 21-dpi lesions of WT and ACAT KO mice. **(E)** Quantification of crystal intensity in 21-dpi lesions of WT and ACAT KO mice by confocal reflection microscopy. **(F–H)** Confocal images of WT microglia and quantification of crystal colocalization with lipid droplets labeled with PLIN2 (yellow) and LAMP1+ lysosomes (red). Examples of colocalization with lysosomes and lipid droplets are highlighted by arrowheads and arrows, respectively. **(I)** Representative TEM pictures of cholesterol crystals in WT and ACAT KO lesions at 21 dpi. WT microglia occasionally showed small crystals (<5 μm, magenta arrowheads), while large crystals (>15 μm) were rarely observed in ACAT KO lesions (magenta arrows). The results are representative of three independent experiments. Scale bars, 2 μm in A, 3 μm in C, and 5 μm in I. *, P < 0.05; **, P < 0.01; ***, P < 0.001. CC, cholesterol crystals; IDA, integrated density area.
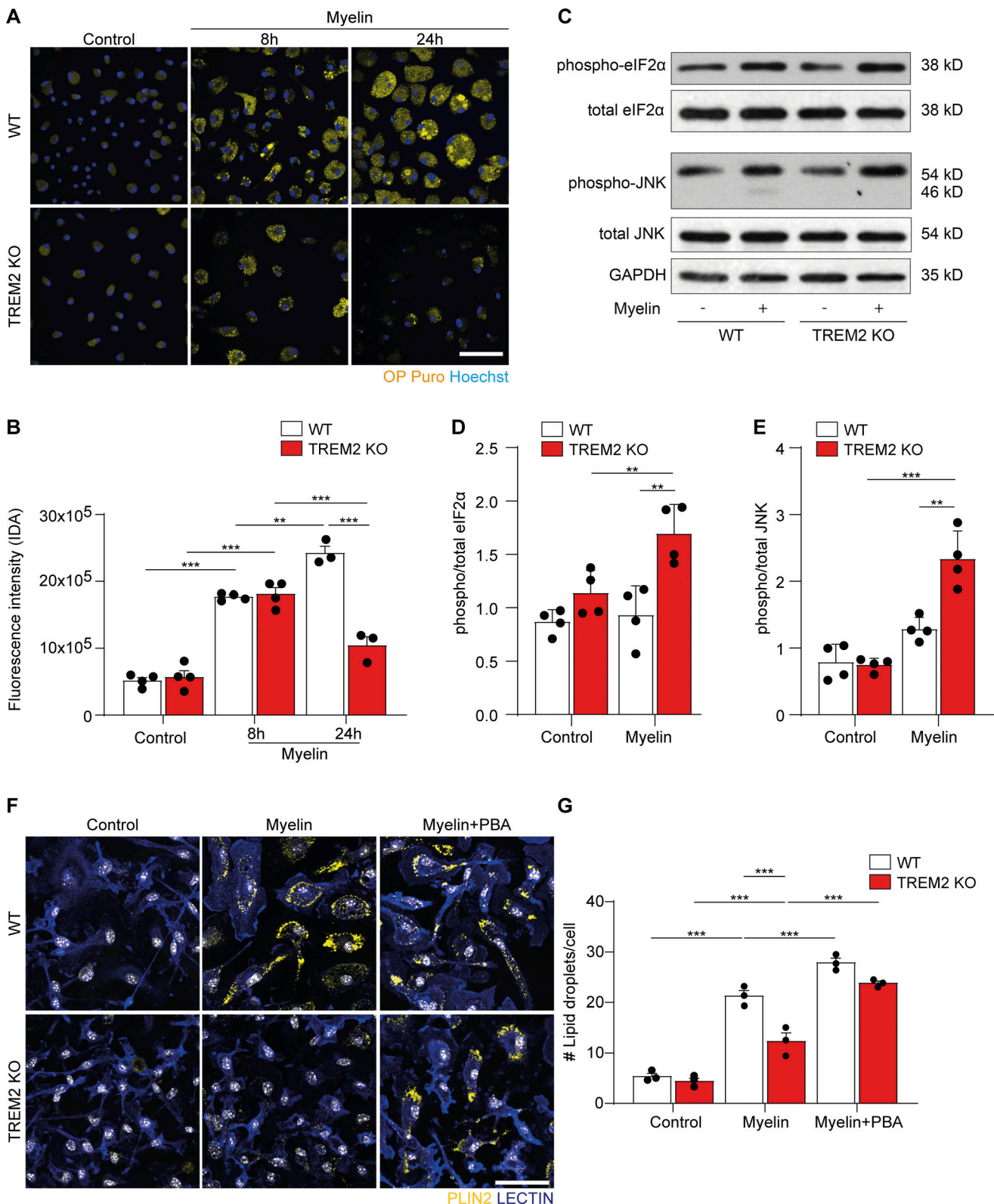
**Figure S3. Myelin phagocytosis causes ER stress in TREM2 KO microglia. (A)** Confocal images of WT and TREM2 KO microglia after treatment with myelin for 8 and 24 h and after incorporation with OP puro (yellow; Hoechst, blue). **(B)** Quantification of the fluorescence intensity per cell of labeled OP puro. **(C–E)** Representative Western blot and quantifications of p-eIF2α and total eIF2α, p-JNK and total JNK, and the housekeeping gene GAPDH. **(F and G)** Representative confocal images and quantification of lipid droplets in WT and TREM2 KO microglia in control conditions and after treatment with myelin for 24 h, with or without 10 μM PBA. Scale bars, 20 μm in A and 25 μm in F. $n = 4$ biological replicates, where at least 40 cells per condition were measured in each condition. For C, D, and E, $n = 4$ biological replicates. The results are representative of three independent experiments. Data represent mean ± SEM. P values were calculated using two-way ANOVA (A) with Šidák post hoc correction. **, $P < 0.01$; ***, $P < 0.001$. IDA, integrated density area.